processes

MDPI

Article

Microwave-Assisted Reduction of Graphene Oxide to Reduced Graphene Oxide

Jessica T. Mhlongo [1], Boitumelo Tlhaole [1], Linda Z. Linganiso [2], Tshwafo E. Motaung [3] and Ella C. Linganiso-Dziike [1,3,4,*]

[1] Molecular Sciences Institute, School of Chemistry, University of the Witwatersrand, Private Bag 3, Johannesburg 2050, South Africa
[2] Institute for Catalysis & Energy Solutions (ICES), Florida Campus, University of South Africa, Johannesburg 1709, South Africa
[3] Department of Chemistry, Sefako Makgatho Health Science University, P.O. Box 94, Medunsa, Ga-Rankuwa, Pretoria 0204, South Africa
[4] Microscopy and Microanalysis Unit, University of the Witwatersrand, Private Bag 3, Johannesburg 2050, South Africa
* Correspondence: cebisa.linganiso@wits.ac.za or linganisoella@gmail.com; Tel.: +27-11-717-1339

Abstract: Green chemistry seeks to find alternative synthesis routes that are less harsh to living organisms and the environment. In this communication, a microwave-assisted hydrothermal technique and a thermal annealing method were used in the reduction of graphene oxide (GO) to make reduced GO (rGO). Graphite powder was oxidised using the Improved Hummers' method, exfoliated, and freeze-dried. Thereafter, an aqueous suspension of GO was reduced under microwave (MW) irradiation for 10 min at 600 W with and without the help of a reducing agent (hydrazine hydrate). Thermal annealing reduction was also conducted under a nitrogen atmosphere at 300 °C for 1 h. Prepared samples were analysed using Raman laser spectroscopy, X-ray diffraction (XRD), transmission electron microscopy (TEM), the Brunauer–Emmett–Teller (BET) method, and X-ray photoelectron spectroscopy (XPS). A successful reduction in the GO functional groups between the sheets was established using XRD. In the Raman analysis, the ratio of the intensity of the D and G band (I_D/I_G) in graphene sheets assisted in assessing the quality of the graphene films. An estimation of the number of structural defects was calculated using the I_D/I_G ratio. The Raman analysis showed an increase in the I_D/I_G ratio after both oxidation and reduction processes. The defect densities of both MW-treated samples were comparable while an increased defect density was evident in the thermally annealed sample. TEM micrographs confirmed the sheet-like morphology of the samples. The rGO sheets obtained from the MW-treated method appeared to be smaller when compared to the rGO ones obtained by thermal treatment. It was also evident from XRD analysis that thermal treatment promoted the coalition of graphitic layers, such that the estimated number of layers was larger than that of GO. The elemental analysis showed that the C/O ratio of GO increased from 2 to 7.8 after MW hydrazine reduction.

Keywords: reduced graphene oxide; microwave assisted reduction; modified Hummers' method; thermal treatment

check for updates

Academic Editor: Nikolay Yu. Peskov

Received: 20 November 2024
Revised: 5 December 2024
Accepted: 9 January 2025
Published: 14 January 2025

Citation: Mhlongo, J.T.; Tlhaole, B.; Linganiso, L.Z.; Motaung, T.E.; Linganiso-Dziike, E.C. Microwave-Assisted Reduction of Graphene Oxide to Reduced Graphene Oxide. *Processes* **2025**, *13*, 216. https://doi.org/10.3390/pr13010216

Copyright: © 2025 by the authors. Licensee MDPI, Basel, Switzerland. This article is an open access article distributed under the terms and conditions of the Creative Commons Attribution (CC BY) license (https://creativecommons.org/licenses/by/4.0/).

1. Introduction

The revolution of graphene material began about twenty years ago when Novoselov's group published a paper on the properties of a graphene material produced from

graphite [1–4]. The exceptional properties of this material, referred to in the paper title a 'wonder material', led to its application in a variety of fields from electronics [5] to clothing [6] and biomedicine [7]. Graphene consists of a single layer of sp^2 hybridised carbon atoms arranged in a 2D honeycomb lattice [1–7]. Some of the extraordinary properties include a high room temperature electron mobility (200,000 $cm^2 \cdot V^{-1} \cdot s^{-1}$), a high current density (2.2 $g \cdot cm^{-1}$), a high optical transparency (97.7%), a high theoretical surface area (2600 $m^2 \cdot g^{-1}$), and a high thermal conductivity (5000 $W \cdot m^{-1} \cdot K^{-1}$) [1–7]. Graphene can be obtained from non-graphitic and graphitic sources [8]. The chemical vapour deposition growth of graphene on various transition metal catalysts (Ir, Ni, Cu, and Co) [5,8–12] and the epitaxial growth of graphene on silicon carbide substrates [13] are methods that employ non-graphitic sources. Graphene obtained using these methods is of high quality and has a large surface area, but these methods are not suitable for large-scale synthesis. Well-documented methods of obtaining graphene from graphitic sources include the unzipping of carbon nanotubes [14], the liquid exfoliation of graphite [15], and chemical oxidation followed by the reduction of graphite [4,16]. A popular and cost-effective method for obtaining graphene is the oxidation of graphite powder using the well-known Hummers' method followed by a reduction step [4,16,17]. Graphite oxide (GrO) is obtained after the chemical oxidation of graphite. Once the GrO is exfoliated, single- or few-layered graphite sheets are obtained with oxygen functional groups on the basal planes and edges known as graphene oxide (GO) [18]. These oxygen functional groups can be removed completely or to some degree using a reduction technique with or without a reducing agent. Reduction without a reducing agent includes reflux in appropriate solvents at a high temperature [19], hydrothermal methods [20], and thermal heating [4,21]. Hydrazine has been reported to be the best reducing agent for GO, producing reduced graphene oxide (rGO) with the lowest carbon-to-oxygen (C/O) ratio and high electrical conductivity [22,23]. In the quest to find a greener alternative, researchers have employed micro-organisms, enzymes, sugars, and other organic compounds as GO-reducing agents [16,24]. Zhang and co-workers [24] were the first to report the use of ascorbic acid (vitamin C) as a green competitive alternative. The rGO produced using vitamin C illustrated electrical conductivities and C/O ratios closest to the hydrazine-synthesised rGO. Some of the recent works where alternative and greener reagents have been used in rGO synthesis are summarised in Table 1. Many green plant-based regents are being explored in the GO-to-rGO reduction process; however, many of these still require prolonged reaction times at elevated temperatures as shown in Table 1. Apart from searching for a greener reducing agent, researchers are also investigating greener reducing strategies for the synthesis of rGO from GO. Microwave technology is considered an efficient technique with appealing reaction times, lower energy consumption, and higher production yields [17,25]. Thus, it has been studied as a viable option for reducing GO [26–28]. The influence of reaction time and power level on the structural and electrical properties of rGO when employing Zn as a reducing agent was studied by Agusu et al. [25]. Elazab [26] and Li [27] produced rGO by both employing an MW-assisted hydrazine reduction method. The obtained C/O ratio was reported as 8.1 and 5.3 for reactions ran at 250 W and 300 W, respectively. This paper reported on the synthesis of rGO from graphite powder. The graphite powder was initially oxidised using the Improved Hummers' method followed by exfoliation and finally reduced using a microwave-assisted hydrothermal method. Hydrazine was used as the common reducing agent while MW treatment without a reducing agent and thermal annealing at 300 °C were employed as less invasive treatments [29].

Table 1. Literature summary of recent works where green reagents were used to reduce GO to rGO.

Method of Reduction	Green Reagent	Application	Reference
Refluxed for 3 h at 85 °C	*Tinospora cordifolia* plant extract	Methyl blue dye degradation Antibacterial activity	[30]
Refluxed for 24 h at 95 °C	*Aloe vera*	Methylene blue dye removal	[31]
Oil bath at 80 °C for 2 h	Lemon Juice and NaOH	Methyl blue absorption	[32]
Stirred at room temperature for 48 h followed by reflux at 100 °C for 24 h	*Azadirachta indica* extract	Hydrogen peroxide electrochemical sensing	[33]
Refluxed at 95 °C for 5 h	*Bougainvillea glabra* flower extract	MB, RhB, MO, and SA degradation Antibacterial activity	[34]
Heat at 95 °C for 12 h	Vitamin C Ammonia solution	Composites	[35]
Water bath at 90 °C	*Chlorella* sp. UMACC 313	Biophotovoltaics	[36]
Heating at 100 °C for 12 h	*Persea americana* mill. extract	Oxygen reduction reaction Antibacterial activity	[37]
Stirred at room temperature for 12 h	Ascorbic acid Ammonia solution	Supercapacitors	[38]
Heat at 70 °C for 24 h	Ellagic acid Tris	Ultrasound contrast agent	[39]
Autoclave treatment at 180 °C for 8 h	-	RhB degradation (with TiO_2)	[40]
Heated at 70 °C for 1 h	*Vernonia Amygdalina* plant leaf extract	-	[41]
Hot water bath for 8 h	*Saraca indica* leaf extract	Antioxidant, antibacterial activity Cytotoxic activity	[42]
Oil bath heating at 60–100 °C and 1–6 h	*Clinacanthus nutans* leaf extract	Electrochemical activity Ecotoxicity	[43]
Refluxed for 24 h	*Pleurotus sajor caju* extract	Antibacterial activity Cytotoxic activity	[44]
Refluxed at 90 °C for 24 h	*Onosma bracteosa* Leaf Extract	Electrochemical sensing	[45]
Autoclave treatment at 100 °C for 12 h	*Plectranthus amboinicus* leaf extract	Supercapacitors	[46]
Reflux at 100 °C for 10 h	*Ocimum sanctum* extract	Cytotoxic activity	[47]

2. Materials and Methods

2.1. Starting Materials

Graphite powder (<20 μm, synthetic), potassium permanganate ($KMnO_4$, 99%), sulfuric acid (H_2SO_4, 98%), phosphoric acid (H_3PO_4, 85%), hydrogen peroxide (H_2O_2, 30%), hydrazine hydrate (N_2H_4, 50–60%), L-ascorbic acid ($C_6H_8O_6$, 99%), and barium chloride dihydrate ($BaCl_2 \cdot 2H_2O$, 96%) were purchased from Sigma Aldrich, Johannesburg, South Africa, and used without any further purification. A 10% hydrochloric acid solution was prepared by diluting a purchased HCl (36%, Sigma Aldrich, South Africa) solution with distilled water.

2.2. Synthesis of GO

The Improved Hummers' method [29,48] was employed for the synthesis of GO. Graphite powder (3 g) and $KMnO_4$ (18 g) were added with stirring to a cold (0 °C) acid mixture containing 360 mL of H_2SO_4 and 40 mL of H_3PO_4. This was done slowly to ensure that the temperature did not exceed 20 °C. This reaction mixture was then stirred for 12 h at 50 °C. The oxidation reaction was terminated by adding 3 mL of H_2O_2 followed by 400 mL of ice-cold distilled water to the GO solution. The brown gel was centrifuge-washed at 15,000 rpm with 10% HCl to remove all sulphate ions (tested using $BaCl_2 \cdot 2H_2O$), followed by washing with distilled water until a pH of ~7 was achieved. The gel was ultra-sonicated for an hour and vacuum freeze-dried at ~−80 °C for a week.

2.3. Reduction of GO

The GO powder (200 mg) was dispersed in 200 mL of distilled water and sonicated to create a suspension. Hydrazine hydrate (1 mL) was added to the suspension and stirred to ensure homogeneity. A second similar GO dispersion was prepared without the addition of hydrazine hydrate. The GO dispersions were transferred into Teflon-lined microwave reaction vessels and placed inside the microwave reactor (Multiwave 3000, Anton Paar, Johannesburg, South Africa) operated at 600 W for 10 min and fan-cooled to room temperature. The black precipitates that were formed were washed with distilled water and ethanol before drying overnight at 100 °C. Another GO sample of 200 mg was thermally reduced for 1 h under a N_2 atmosphere in a horizontal tube furnace at 300 °C and a 20 mL/min N_2 flow rate.

The rGO products were labelled as H-rGO and C-rGO for the samples prepared by MW using hydrazine hydrate and no reducing agent, respectively, and the thermal-treated sample was labelled T_N-rGO.

2.4. Characterisation

The phase characteristics of the as-synthesised GO and rGO powders were determined by powder X-ray diffraction (Bruker D2 phaser diffractometer) in the scan range $5° \leq 2\theta \leq 90°$ with a 0.02° measurement step, using a Cu-Kα (λ = 0.154 nm) radiation source. Raman measurements were conducted on a Horiba LabRAM Raman spectrometer equipped with an Olympus BX41 microscope attachment. The morphological properties of the samples were established using a transmission electron microscope with an acceleration voltage of 120 keV (Tecnai Spirit T12, Johannesburg, South Africa). The thermo-gravimetric analysis (TGA) of the rGO samples was performed from 35 to 900 °C under air (10 mL/min) at a heating rate of 10 °C/min (TGA 4000, Perkin Elmer, Johannesburg, South Africa). N_2 adsorption and desorption isotherms were recorded using a Micrometrics Tristar 3000 (Johannesburg, South Africa) instrument at 77 K after degassing the samples at 423–473 K in N_2. The specific surface area and the pore size distribution of the samples were acquired using the Brunauer–Emmet–Teller (BET) equation and the Barrett–Joyner–Halenda (BJH)

method, respectively. The chemical composition of the GO and rGO samples was determined by X-ray photoelectron spectroscopy (XPS) using a monochromatic Al Kα source operated at 1486.7 eV (Physical Electronics Quantum 2000, Pretoria, South Africa).

3. Results and Discussion

3.1. Phase Composition

The X-ray diffractograms of graphite, GO, and the rGO products are shown in Figure 1. Graphite (Figure 1a, inset) displayed diffraction peaks at 2θ = 26.4°, 42.4°, 44.4°, and 54.4° ascribed to the (002), (100), (101), and (004) planes of carbon (JCPSD 00-008-0415), respectively. The (002) peak corresponded to an interlayer spacing of 0.34 nm as shown in Table 2. After oxidation, all of the peaks in the graphite disappeared except the (100) plane, and a new peak emerged at 2θ = 10.9° corresponding to the (001) plane of carbon, consistent with an interlayer spacing of 0.87 nm (Figure 1a and Table 2). The increase in interlayer spacing can be attributed to an expansion between the graphitic layers due to the incorporated oxygen functional groups on the graphite sheets [48]. The (001) plane was also wider than the (002) peak in graphite, suggesting a decrease in the crystallinity of the carbon framework. Nevertheless, it was distinct and sharp, especially when compared to the rGO profiles, suggesting that the ordered structure along the c-axis was preserved [49]. The reduction process caused a re-appearance of the (002) plane and disappearance of the (001) plane, with a decreased interlayer spacing of 0.37 nm for H-rGO and C-rGO and 0.35 nm for T_N-rGO (Figure 1b and Table 2). The interlayer spacing in all three rGO samples suggested that the degree of oxygen functional group removal between the sheets was similar. Additionally, the (002) plane in all the rGO samples was wider due to poor ordering along the stacking direction, also suggesting that the rGO consisted mostly of freestanding graphene sheets [50]. Most importantly, it is clear from these results that the MW heating method is able to perform GO reduction to rGO without any additional reducing agent, presenting a green alternative to rGO synthesis. Voiry et al. explained in their study that the conductive GO absorbs microwaves, causing an accelerated heating of the GO and leading to the desorption of oxygen functional groups and the re-arrangement of the graphene basal plane [28].

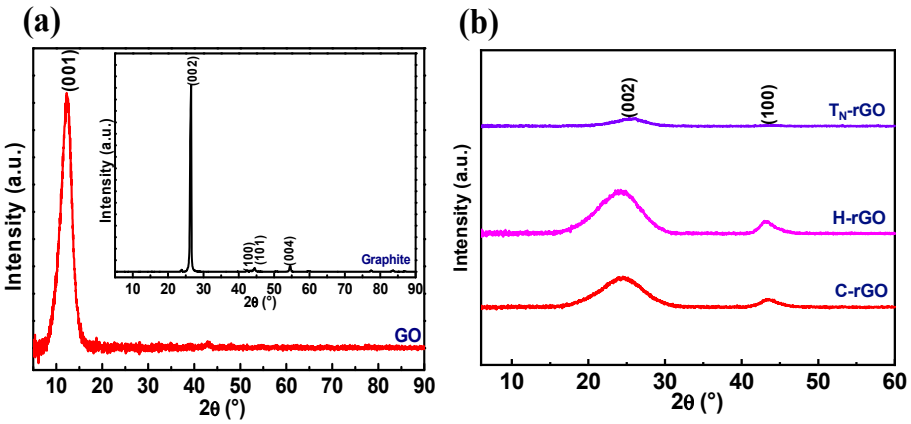


Figure 1. X-ray diffractograms for (**a**) GO (inset: graphite) and (**b**) rGO samples.

The crystal stack height (L_c) and the number of graphene layers in the crystal (N_c) were estimated using Equations (1) and (2) [16], and the data are summarised in Table 2.

$$L_c = \frac{k_1 \lambda}{\mathrm{FWHM}\cos\theta_1} \quad (1)$$

$$N_c = \frac{L_c}{d_{002}} \quad (2)$$

where, λ is the radiation wavelength, θ_1 the diffraction peak position for either the (002) or (001) diffraction plane, k_1 is a form factor usually applied as 0.9, and FWHM the width at half-height for the corresponding plane.

The oxidation and reduction processes produced a decrease in the crystal domain (L_c), implying an increase in the structural disorder of GO and rGO. The number of layers (N_c) also decreased significantly after oxidation and exfoliation. The estimated number of graphene layers in GO was one layer higher than that in H-rGO and A-rGO, while one layer less than that in T_N-rGO. The stacking height (L_c) of GO was significantly higher than those in the rGO samples, where the L_c for T_N-rGO > H-rGO > C-rGO. This may be attributed to the presence of the oxygen moieties in between the graphene sheets of the GO. The decreased stacking height could also serve a further confirmation of the removal of oxygen functional groups between the graphene sheets resulting in the rearrangement of the carbon structure in the rGO. The increased number of layers for the thermally annealed sample suggests the possibility of a coming together of the sheets under the employed treatment conditions. A recent report showed a growth of 2D graphene-like layers from heat treatment of carbon dots between 200 and 700 °C [51].

Table 2. Powder XRD data on graphite, GO, and rGO samples.

	Plane (002) or (001) (2 θ(°))	**L_c (nm)**	**d_{002} or d_{001} (nm)**	**N_c**
Graphite	26.4	19.4	0.34	57
GO	10.2	3.35	0.87	4
H-rGO	24	1.29	0.37	3
C-rGO	24.3	1.26	0.37	3
T_N-rGO	25.3	1.73	0.35	5

3.2. Structural Properties

Raman spectroscopy is a powerful tool for evaluating the degree of graphitisation of carbon materials [52,53]. Raman spectra obtained from graphite and GO are presented in Figure 2a. The main characteristic peaks observed in graphite at 1352, 1579, and 2716 cm^{-1} belonged to the D, G, and 2D bands, respectively. The disorder-induced D band had a very low intensity in the graphite sample, implying a low concentration of defects in the carbon structure [54]. However, after oxidation, the intensity and area of this band increased due to the transformation of some sp^2-carbons into sp^3-carbons upon the incorporation of oxygen functionalities. Additionally, the D band shifted upward to 1359 cm^{-1}. The G band was instigated by the first-order Raman scattering processes attributed to the in-plane vibrational modes of the sp^2-hybridised carbon at the graphene basal planes [50,53]. After oxidation, the G band shifted to a higher wavenumber (1590 cm^{-1}), and the area under the band increased notably. The FWHM is usually used to describe the crystallinity of carbon materials: a smaller FWHM implies better crystallinity [55]. This supports the XRD data suggesting a decrease in the crystallinity from graphite to GO. The 2D band is produced by the double resonance process including the intervalley scattering by two in-plane transverse optical (TO) phonons near the K point of the Brillouin zone [52,53]. The intensity of this band was very weak in the GO, probably due to the chemically induced defects [56]. The rGO spectra (Figure 2b) showed prominent D and G bands in all three rGO samples. The D band shifted to lower wavenumbers in all the reduced samples except for T_N-rGO, which shifted to higher wavenumbers; however, the G band continued to shift to higher wavenumbers for all the reduced samples. The shift in positions could be

associated with strain in the carbon structure due to the removal of the oxygen groups during the reduction process. There was also a decrease in the FWHM of both the D and G bands in the MW-treated rGO samples, while the G band for T_N-rGO remained the same as that in the GO, and the D band was higher than those in all the samples.

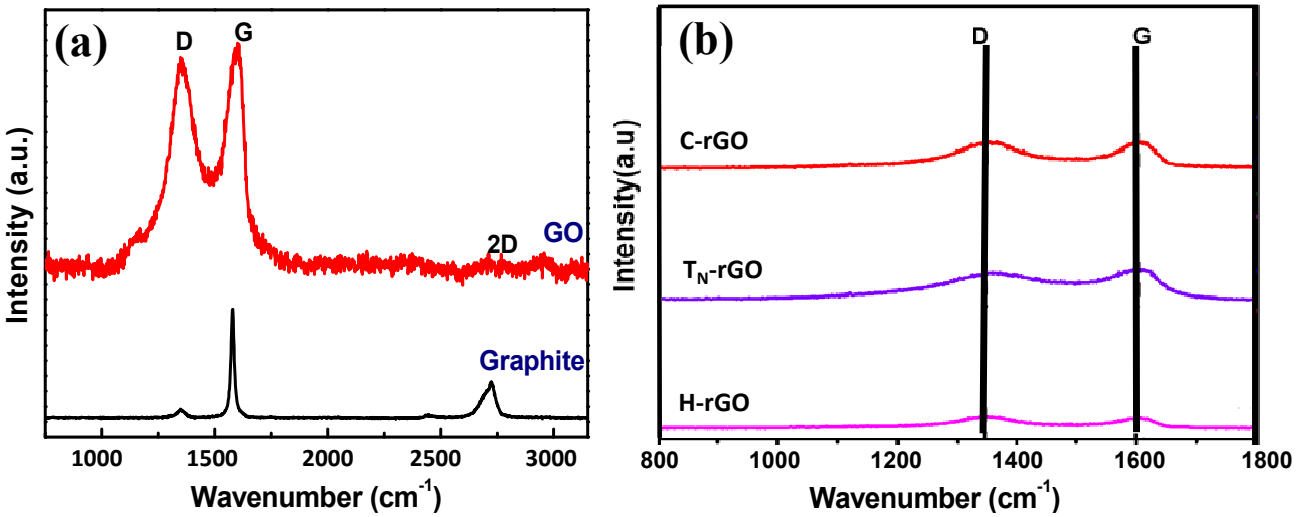


Figure 2. Raman spectra of (**a**) graphite and GO and (**b**) rGO samples.

The ratio of the intensity of the D and G bands (I_D/I_G) in graphene sheets assists in assessing the quality of the graphene films [50]. An estimation of the number of structural defects was calculated using the I_D/I_G ratio (the area under the peaks was used instead of the relative intensities) and is presented in Table 3. The estimated concentration of defects increased after oxidation and reduction, indicating that the graphene sheets were highly defective. The defects in the sample reduced by thermal treatment were higher than those in the H-rGO sample, and the defect concentrations in C-rGO were slightly lower than those in the H-rGO sample. This observation further confirms that the MW treatment efficiently reduces the GO to rGO without the need for a chemical reducing agent under the reaction parameters used. It was further demonstrated that thermal treatment at 300 °C in a nitrogen environment also reduced Go to rGO. The higher estimated defect concentration in TN-rGO may be attributed to the removal of intercalated water molecules from the GO as well as a removal of residual oxygen functionalities that have a lower binding energy such as hydroxyl groups in the form of water vapour during thermal treatment [57]. A TGA analysis was performed on the rGO sfamples (Figure S1), and it was observed that C-rGO had the lowest decomposition temperature at 567 °C, followed by T_N-rGO at 590 °C, and H-rGO had the highest decomposition temperature at 601 °C. The higher thermal stability in H-rGO may be attributed to the introduction of nitrogen groups into the carbon matrix during the reduction process. The difference between the thermal stabilities in all the prepared rGO samples was less than 35 °C, and it was comparable to the reported data [58].

Table 3. Raman peak positions for graphite, GO, and rGO samples.

Sample	D Band		G Band		2D Band	ID/IG
	Centre (cm^{-1})	FWHM (cm^{-1})	Centre (cm^{-1})	FWHM (cm^{-1})	Centre (cm^{-1})	
Graphite	1352	30	1579	16	2716	0.17
GO	1359	143	1590	82	-	1.63

Table 3. *Cont.*

Sample	D Band		G Band		2D Band	ID/IG
	Centre (cm^{-1})	FWHM (cm^{-1})	Centre (cm^{-1})	FWHM (cm^{-1})	Centre (cm^{-1})	
H-rGO	1350	127	1597	62	-	2.23
C-rGO	1352	137	1596	65	-	2.13
T_N-rGO	1364	221	1592	82	-	2.51

3.3. Morphology Analysis

TEM micrographs were used to study the morphology of the materials. Graphite displayed a crystalline platelet-like morphology with well-defined sheets (Figure 3a). GO and rGO also displayed a sheet-like morphology with a size of a few micrometres (Figure 3b–e). The wrinkles present in the GO sheets (Figure 3b) were due to the transformations in the electronic structure of the carbon atoms where the hybridisation changed from sp^2 to sp^3 after the incorporation of oxygen moieties [59]. The wrinkling persisted in rGO (Figure 3c–e) due to the defects associated with pores, holes, and cavities introduced during the reduction process and the strain in the carbon–carbon bonds [54]. A difference between the rGO samples was noted where the T_N-rGO showed larger sheets when compared with the samples prepared via MW treatment. The mechanism of reduction during thermal treatment did not involve the constant stirring of the GO; as a result, less breakage in the graphene sheets can be observed.

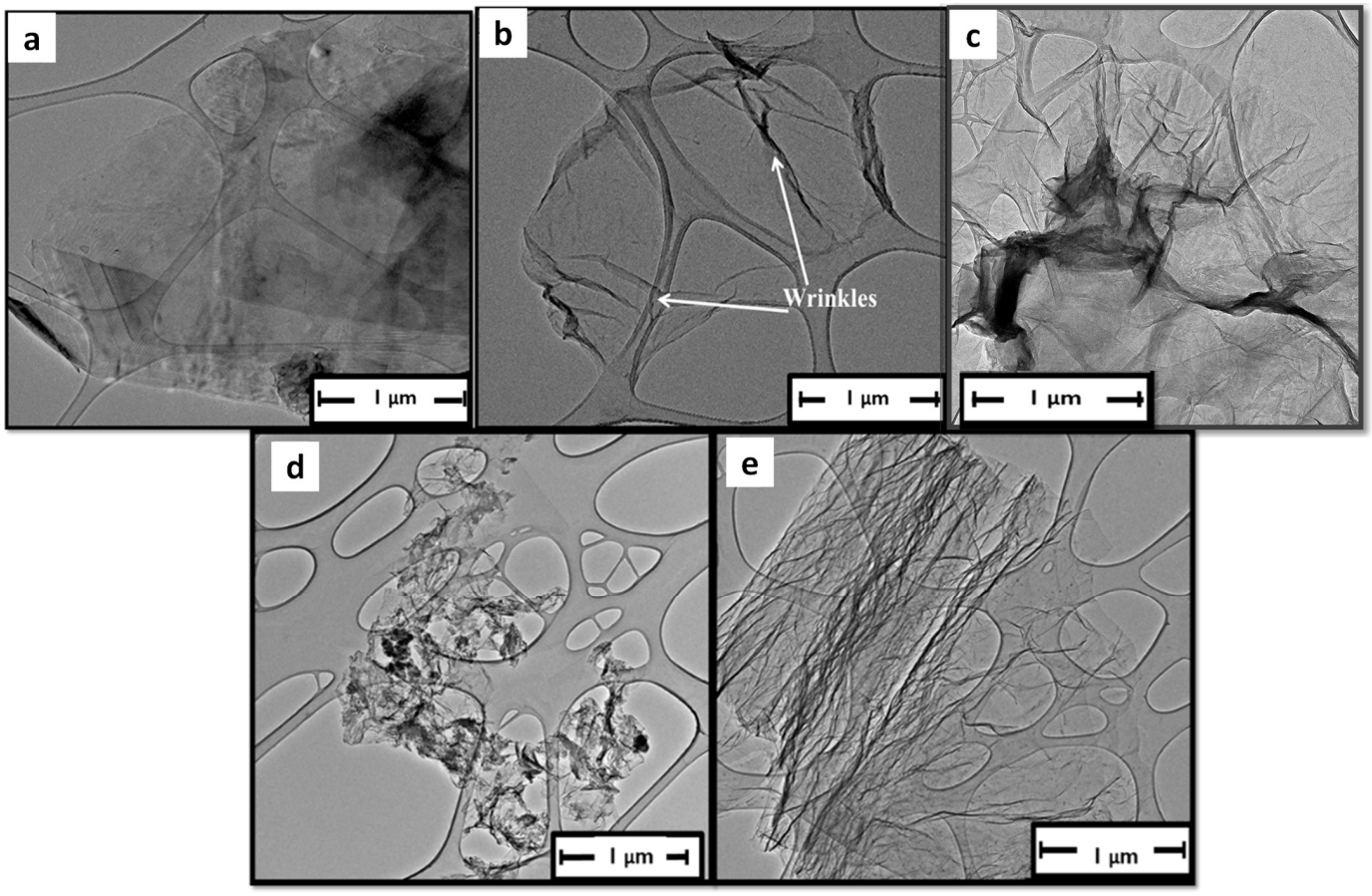


Figure 3. TEM micrographs of (**a**) graphite, (**b**) GO, (**c**) H-rGO, (**d**) C-rGO, (**e**) and T_N-rGO.

3.4. Textual Properties

The N_2 adsorption–desorption isotherms of graphite, GO, and H-rGO are illustrated in Figure 4. Graphite exhibited a type III isotherm with an H3 hysteresis loop (Figure 4a), while GO and H-rGO showed a type IV isotherm also with an H3 hysteresis loop (Figure 4b,c). The surface area of the graphite increased from 6.9 m^2/g to 80.4 m^2/g after oxidation as shown if Table 4. This increase can be attributed to the chemical oxidation followed by exfoliation via sonication. After reduction, there was a further increase in the surface area to 815.2 m^2/g (Table 4). As the graphitic structure collapsed further, the specific surface area increased. This surface area was less than the theoretical surface area of graphene (2600 m^2/g) due to some degree of agglomeration in the sheets; however, it was also much higher than the surface area of the rGO obtained via MW treatment (439 m^2/g [60]) and hydrothermal treatment (364 m^2/g [61]) by other researchers. The pore diameter distribution curves for all three samples were included as inserts in their respective BET isotherms. Narrow peaks were observed centred at ~3.4 nm for both GO and H-rGO, whereas there was a broad peak centred at 137.5 nm for graphite. These suggest that GO and H-rGO have mesopores while graphite has micropores. The pore distribution between 90 and 160 nm in graphite can be attributed to the spacing between the bulk graphite structure.

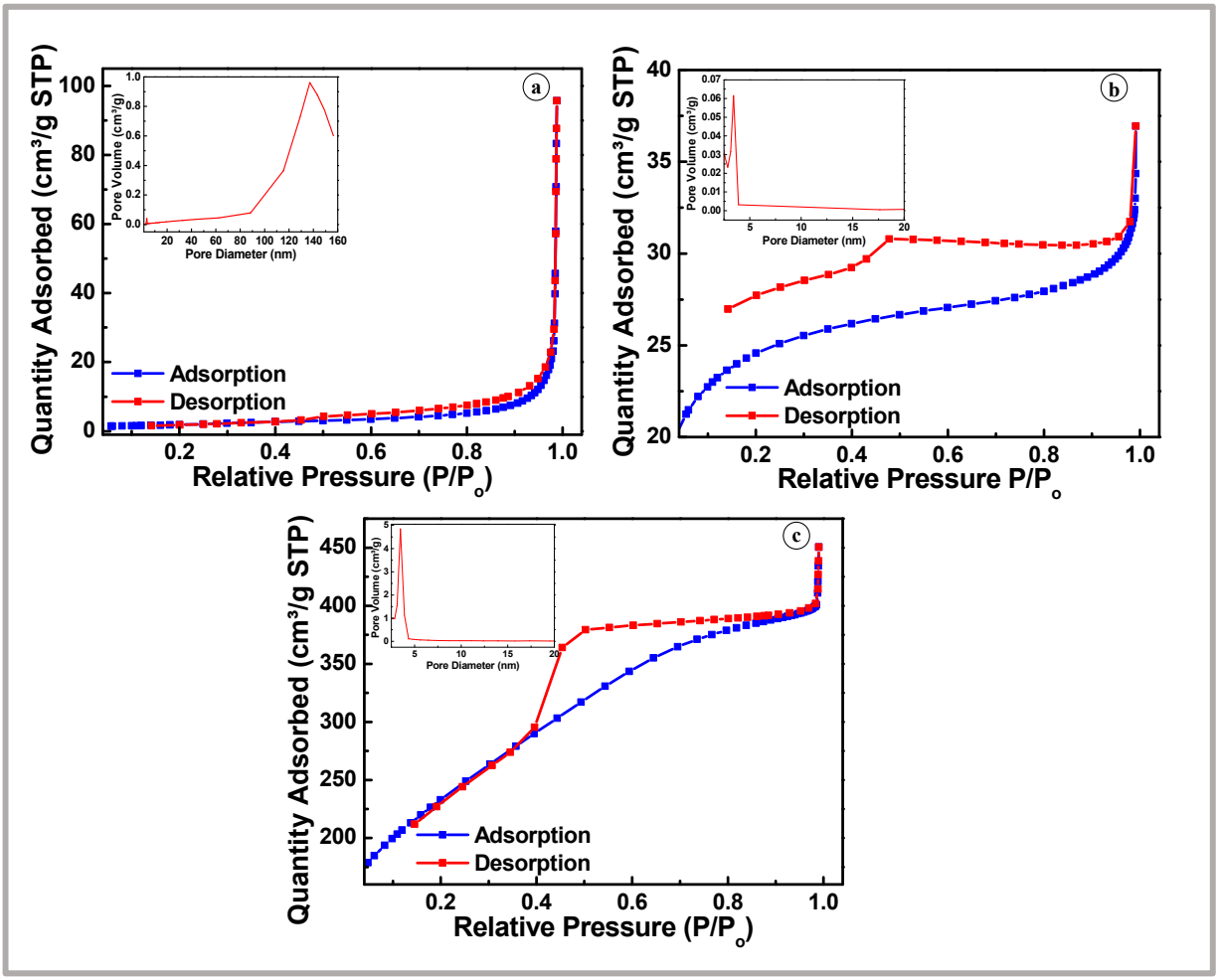


Figure 4. N_2 adsorption–desorption isotherms and their respective pore diameter distribution curves (inset) for graphite (**a**), GO (**b**), and H-rGO (**c**).

Table 4. Surface area data for graphite, GO, and H-rGO.

Sample	BET Surface Area (m^2/g)	Pore Volume (cm^3/g)
Graphite	6.9	0.15
GO	80.4	0.02
H-rGO	815.6	0.61

3.5. Elemental Analysis

The surface composition and carbon hybridisation of GO and H-rGO were studied with XPS. Figure 5 shows that the survey spectra of GO consisted of C 1s (~284 eV) and O 1s (~531 eV). In addition to the C 1s and O 1s, the survey spectra of H-rGO also exhibited a weak N 1s peak at approximately 398 eV.

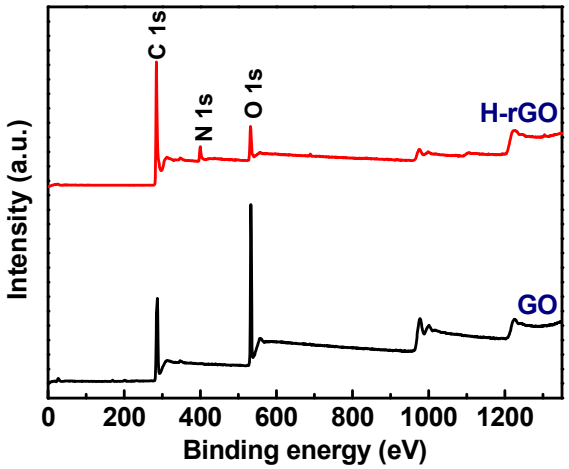


Figure 5. XPS survey spectra of GO and H-rGO.

The integrated areas under the peaks gave an estimation of the atomic percentages of each element in the prepared materials (Table 5). A decrease in oxygen content from GO (33.2 at %) to H-rGO (10.6 at %) was observed, indicating a successful reduction. The carbon content increased after reduction, making the C/O ratio in H-rGO 7.8. This C/O ratio was similar to that in the MW-assisted hydrazine reduction by Elazab [27]. Furthermore, approximately 6.8 at % of nitrogen was present, arising from the hydrazine hydrate used during reduction [23]. Low atomic percentages of impurities were present in both GO and H-rGO.

Table 5. Atomic compositions of GO and H-rGO.

	C (at %)	O (at %)	N (at %)	S (at %)	Cl (at %)	F (at %)	Mg (at %)
GO	66.1	33.2	-	0.4	0.2	-	-
H-rGO	82.2	10.6	6.8	-	-	0.3	0.2

The high-resolution C 1s XPS spectra of both GO and H-rGO (Figure 6a,b) were used to determine the chemical environments of the C atoms. In both samples, the C 1s spectra were deconvoluted into four peaks. The deconvoluted C 1s spectra displayed peaks at ~284 eV, ~287.2 eV, ~287.4 eV, and ~289.2 eV, corresponding to the sp^2 and defective sp^3 C-C bonds; epoxy and hydroxyl; carbonyl; and carboxyl groups, respectively [62]. After reduction, the peak positions for most of the oxygenated carbon atoms shifted to lower bonding energies due to the bonding of the carbon atoms to the electronegative

nitrogen atoms [63]. Additionally, the carbonyl group was replaced with a C-N bond at 285.2 eV. The O 1s spectra for GO (Figure 6c) were deconvoluted into a peak at ~531 eV and ~533 eV, which corresponded to C=O and C-O oxygen functional groups. The intensity of the O 1s peak decreased tremendously after the reduction, as most oxygen single-bonded carbon groups were removed. The deconvoluted N 1s spectra in Figure S2 showed that the nitrogen environment consisted of three configurations, i.e., pyridinic (~399.2 eV), pyrrolic (~400.6 eV), and graphitic (~401.5 eV).

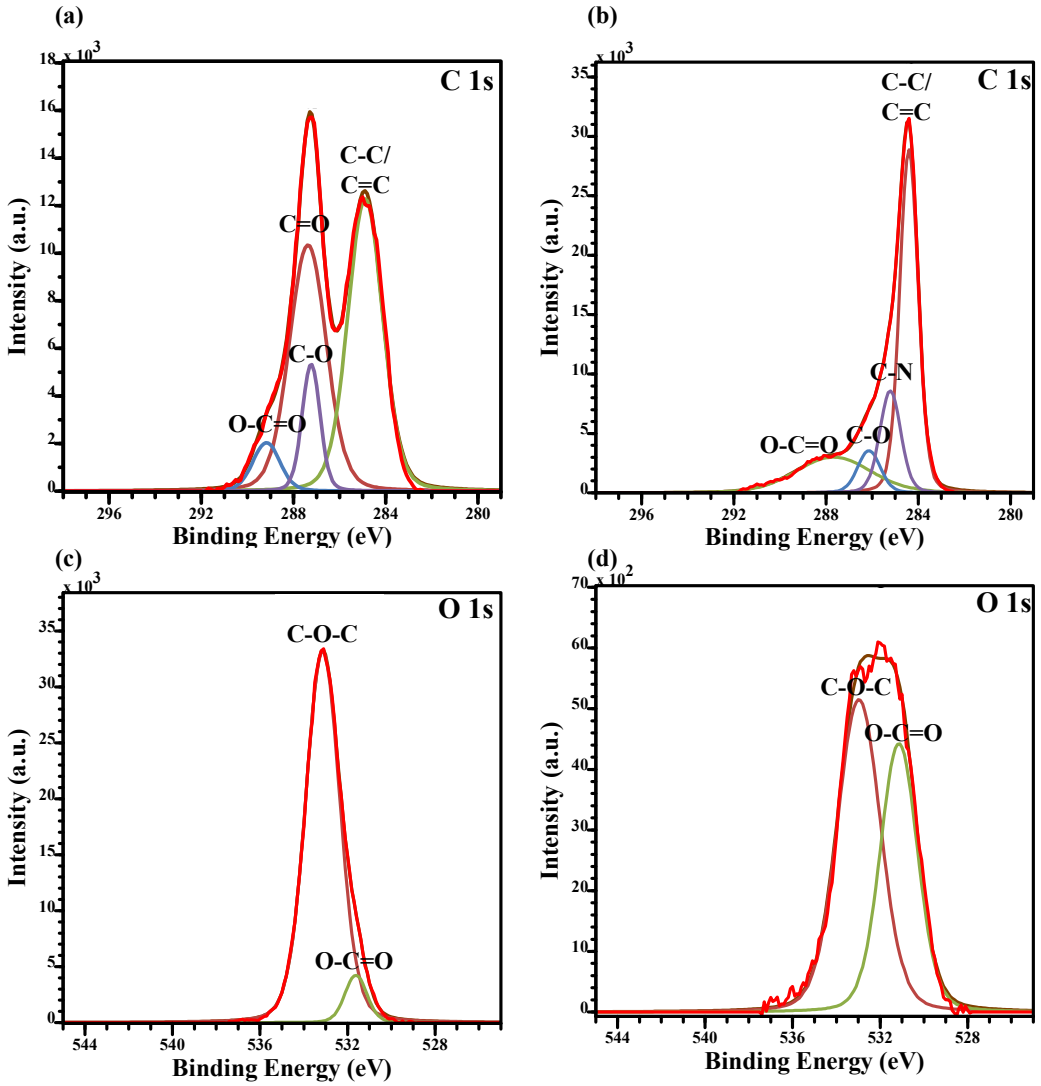


Figure 6. High-resolution XPS spectra of deconvoluted C 1s and O 1s for GO (**a**,**c**) and H-rGO (**b**,**d**).

4. Conclusions

Herein, the effective reduction of GO using a microwave-assisted hydrothermal reduction method as an environmentally benign reduction strategy was demonstrated. Both the MW and thermal reduction procedures produced an rGO that was comparable to hydrazine-hydrate-reduced rGO. The thermal treatment produced less wrinkled sheets that appeared to increase in size and the number of layers, suggesting a coming together of the sheets at 300 °C. All rGO samples demonstrated a clear change in interlayer spacing and stacking when compared to graphite and GO ones. The Raman data illustrated that MW reduction with no reducing agent induced a similar concentration of defects in the carbon structure as that in the H-rGO. The prepared rGO samples also showed a good thermal stability that was comparable to that in the literature data. Further analysis showed that

H-rGO had a C/O ratio of 7.8 and a surface area of 816 $m^2 \cdot g^{-1}$. This study presents a quick, cost-effective, and environmentally friendly alternative to rGO synthesis. The produced rGO showed comparable properties to rGO produced from a commonly used reagent and thermal treatment.

5. Limitations of the Study

This study focused on the MW application in the reduction process of GO to rGO using the commonly used and environmentally unfriendly hydrazine hydrate, comparing it to rGO produced without the use of a reducing agent. The study employed some common techniques to characterise the produced rGO, however, a further application of the produced materials in electronics, biomedicine, and composites would better qualify the prepared rGO. The study did not reveal the impact of microwave heating during a large-scale synthesis of rGO. This limits the scope with regards to possible industrial applications of this process. Future studies should evaluate the effect of reducing reagent concentrations on the rGO. An in situ microwave analysis of the reagents can help determine the active components during the reduction process. The mechanism of GO reduction under MW heating needs to be studied in order to optimise the process for high-quality rGO production, good yield, and upscaling approaches.

Supplementary Materials: The following supporting information can be downloaded at: https://www.mdpi.com/article/10.3390/pr13010216/s1, Figure S1: Thermal decomposition curve of the prepared rGO samples; Figure S2: XPS spectra of N 1s of H-rGO.

Author Contributions: Conceptualisation, E.C.L.-D.; writing—original draft preparation, J.T.M. and B.T.; writing—review and editing, B.T., E.C.L.-D., L.Z.L. and T.E.M. All authors have read and agreed to the published version of the manuscript.

Funding: This research was funded by the National Research Foundation of South Africa (UID 114232 and 129532) and the University of the Witwatersrand. This work is based on the research supported in part by the WITS Chancellor's Female Academic Leaders Fellowship.

Data Availability Statement: The original contributions presented in this study are included in the article/Supplementary Materials. Further inquiries can be directed to the corresponding author.

Conflicts of Interest: The authors declare no conflicts of interest.

References

1. Novoselov, K.S.; Geim, A.K.; Morozov, S.V.; Jiang, D.; Zhang, Y.; Dubonos, S.V.; Grogorieva, I.V.; Firsov, A.A. Electric field effect in atomically thin carbon films. *Science* **2004**, *306*, 666–669. [CrossRef] [PubMed]
2. Geim, A.K.; Novoselov, K.S. The rise of graphene. *Nat. Mater.* **2007**, *6*, 183–191. [CrossRef] [PubMed]
3. Geim, A.K. Graphene: Status and Prospects. *Science* **2009**, *324*, 1530–1534. [CrossRef] [PubMed]
4. De Silva, K.K.H.; Huang, H.-H.; Joshi, R.K.; Yoshimura, M. Chemical reduction of graphene oxide using green reductants. *Carbon* **2017**, *119*, 190–199. [CrossRef]
5. Hu, C.; Song, L.; Zhang, Z.; Chen, N.; Feng, Z.; Qu, L. Tailored graphene systems for unconventional applications in energy conversion and storage devices. *Energy Environ. Sci.* **2015**, *8*, 31–54. [CrossRef]
6. Molina, J. Graphene-based fabrics and their applications: A review. *RSC Adv.* **2016**, *6*, 68261–68291. [CrossRef]
7. Pattnaik, S.; Swain, K.; Lin, Z. Graphene and graphene-based nanocomposites: Biomedical applications and biosafety. *J. Mater. Chem. B* **2016**, *4*, 7813–7831. [CrossRef]
8. Lim, J.Y.; Mubarak, N.M.; Abdullah, E.C.; Nizamuddin, S.; Khalid, M. Recent trends in the synthesis of graphene and graphene oxide based nanomaterials for removal of heavy metals—A review. *J. Ind. Eng. Chem.* **2018**, *66*, 29–44. [CrossRef]
9. Guermoune, A.; Chari, T.; Popescu, F.; Sabri, S.S.; Guillemette, J.; Skulason, H.S.; Szkopek, T.; Siaj, M. Chemical Vapor Deposition Synthesis of Graphene on Copper with Methanol, Ethanol, and Propanol Precursors. *Carbon* **2011**, *49*, 4204–4210. [CrossRef]
10. Coraux, J.; N'Diaye, A.T.; Busse, C.; Michely, T. Structural Coherency of Graphene on Ir(111). *Nano Lett.* **2008**, *8*, 565–570. [CrossRef] [PubMed]

11. Reina, A.; Thiela, S.; Jia, X.; Bhaviripudi, S.; Dresselhaus, M.S.; Schaefer, J.A.; Kong, J. Growth of large-area single- and bi-layer graphene by controlled carbon precipitation on polycrystalline Ni surfaces. *Nano Res.* **2009**, *2*, 509–516. [CrossRef]
12. Ago, H.; Ito, Y.; Mizuta, N.; Yoshida, K.; Hu, B.; Orofeo, C.M.; Tsuji, M.; Ikedi, K.; Mizuno, S. Epitaxial Chemical Vapor Deposition Growth of Single-Layer Graphene over Cobalt Film Crystallized on Sapphire. *ACS Nano* **2010**, *4*, 7407–7414. [CrossRef]
13. Son, I.; Hwan Park, J.; Kwon, S.; Park, S.; Rümmeli, M.H.; Bachmatiuk, A.; Song, H.J.; Ku, J.; Choi, J.W.; Choi, J.; et al. Silicon carbide-free graphene growth on silicon for lithium-ion battery with high volumetric energy density. *Nat. Commun.* **2015**, *6*, 7393. [CrossRef]
14. Yang, X.; Dou, X.; Rouhanipour, A.; Zhi, L.; Rader, H.J.; Mullen, K. Two-Dimensional Graphene Nanoribbons. *J. Am. Chem. Soc.* **2008**, *130*, 4216–4217. [CrossRef] [PubMed]
15. Li, D.; Muller, M.B.; Gilje, S.; Kaner, R.B.; Wallace, G.G. Processable aqueous dispersions of graphene nanosheets. *Nat. Nanotechnol.* **2008**, *3*, 101–105. [CrossRef] [PubMed]
16. Lavin-Lopez, M.P.; Paton-Carrero, A.; Sanchez-Silva, L.; Valverde, J.L.; Romero, A. Influence of the reduction strategy in the synthesis of reduced graphene oxide. *Adv. Powder Technol.* **2017**, *28*, 3195–3203. [CrossRef]
17. Xie, X.; Zhou, Y.; Huang, K. Advances in Microwave-Assisted Production of Reduced Graphene Oxide. *Front. Chem.* **2019**, *7*, 355. [CrossRef] [PubMed]
18. Dreyer, D.R.; Park, S.; Bielawski, C.W.; Ruoff, R.S. The chemistry of graphene oxide. *Chem. Soc. Rev.* **2010**, *39*, 228–240. [CrossRef]
19. Kim, S.; Choi, K.; Park, S. Solvothermal reduction of graphene oxide in dimethylformamide. *Solid State Sci.* **2016**, *61*, 40–43. [CrossRef]
20. Zheng, X.; Peng, Y.; Yang, Y.; Chen, J.; Tian, H.; Cui, X.; Zheng, W. Hydrothermal reduction of graphene oxide; effect on surface-enhanced Raman scattering. *J. Raman Spectrosc.* **2017**, *48*, 97–103. [CrossRef]
21. Jung, I.; Dikin, D.A.; Piner, R.D.; Ruoff, R.S. Tunable electrical conductivity of individual graphene oxide sheets reduced at "low" temperatures. *Nano Lett.* **2008**, *8*, 4283–4287. [CrossRef]
22. Park, S.; An, J.; Potts, J.R.; Velamakanni, A.; Murali, S.; Ruoff, R.S. Hydrazine-reduction of graphite- and graphene oxide. *Carbon* **2011**, *49*, 3019–3023. [CrossRef]
23. Stankovich, S.; Dikin, D.A.; Piner, R.D.; Kohlhaas, K.A.; Keinhammes, A.; Jia, Y.; Wu, Y.; Nguyen, S.T.; Ruoff, R.S. Synthesis of graphene-based nanosheets via chemical reduction of exfoliated graphite oxide. *Carbon* **2007**, *45*, 1558–1565. [CrossRef]
24. Zhang, J.; Yang, H.; Shen, G.; Zhang, J.; Guo, S. Reduction of graphene oxide via L-ascorbic acid. *Chem. Commun.* **2010**, *46*, 1112–1114. [CrossRef] [PubMed]
25. Agusu, L.; Anggara, D.; Mitsudo, S.; Fujii, Y.; Kikuchi, H. Microwave Hydrothermal Synthesis of Reduced Graphene Oxide: Effects of Microwave Power and Irradiation Time. *J. Phys. Conf. Ser.* **2018**, *1011*, 012012. [CrossRef]
26. Elazab, H.A.; Siamaki, A.R.; Moussa, S.; Gupton, B.F.; El-Shall, M.S. Highly efficient and magnetically recyclable graphene-supported Pd/Fe_3O_4 nanoparticle catalysts for Suzuki and Heck cross-coupling reactions. *Appl. Catal. A Gen.* **2015**, *491*, 58–69. [CrossRef]
27. Li, J.; Yang, Z.; Qiu, H.; Dai, Y.; Zheng, Q.; Zheng, G.-P.; Yang, J. Microwave-assisted simultaneous reduction and titanate treatment of graphene oxide. *J. Mater. Chem. A* **2013**, *1*, 11451–11456. [CrossRef]
28. Voiry, D.; Yang, J.; Kupferberg, J.; Fullon, R.; Lee, C.; Jeong, H.Y.; Shin, H.S.; Chhowalla, M. High-quality graphene via microwave reduction of solution-exfoliated graphene oxide. *Science* **2016**, *353*, 1413–1416. [CrossRef]
29. Tlhaole, B. Synthesis of Nickel Sulfide-Reduced Graphene Oxide for Application in Gas Sensors. Master's Dissertation, University of the Witwatersrand, Johannesburg, South Africa, 2020. Available online: https://wiredspace.wits.ac.za (accessed on 1 August 2020).
30. Saini, R.; Mishra, R.K.; Kumar, P. Green Synthesis of Reduced Graphene Oxide Using the Tinospora cordifolia Plant Extract: Exploring Its Potential for Methylene Blue Dye Degradation and Antibacterial Activity. *ACS Omega* **2024**, *9*, 20304–20321. [CrossRef]
31. Bhattacharya, G.; Sas, S.; Wadhwa, S.; Mathur, A.; McLaughlin, J.; Roy, S.S. *Aloe vera* assisted facile green synthesis of reduced graphene oxide for electrochemical and dye removal application. *RSC Adv.* **2017**, *7*, 26680–26688. [CrossRef]
32. Mahiuddin, M.; Ochiai, B. Lemon Juice Assisted Green Synthesis of Reduced Graphene Oxide and Its Application for Adsorption of Methylene Blue. *Technologies* **2021**, *9*, 96. [CrossRef]
33. Kumar, G.G.; Babu, K.J.; Nahm, K.S.; Hwang, Y.J. A facile one-pot green synthesis of reduced graphene oxide and its composites for non-enzymatic hydrogen peroxide sensor applications. *RSC Adv.* **2014**, *4*, 7944–7951. [CrossRef]
34. Das, R.S.; Lingait, D.; Gaharwar, S.S.; Kumar, A.; Gokhale, S. Green synthesis of reduced graphene oxide with multiple environmental applications. *J. Photochem. Photobiol. A Chem.* **2023**, *444*, 115021. [CrossRef]
35. Mindivan, F.; Goktas, M. Green synthesis of Reduced Graphene Oxide (RGNO)/Polyvinylchloride (PVC) composites and their structural characterization. *Mater. Res. Proc.* **2018**, *8*, 143–151. [CrossRef]
36. Tee, J.Y.; Ng, F.L.; Keng, F.S.L.; Lee, C.W.; Zhang, B.; Lin, S.; Kumar, G.G.; Phang, S.M. Green synthesis of reduced graphene oxide by using tropical microalgae and its application in biophotovoltaic devices. *iScience* **2023**, *27*, 109564. [CrossRef]

37. Zikalala, N.E.; Lekhetho, S.A.; Mpeta, S.; Ahmed, R.; Dube, A.; Mketo, N.; Zinatizadeh, A.A.; Mokrani, T.; Maaza, M.M. Green synthesis of reduced graphene oxide using *Persea americana* mill. extract: Characterization, oxygen reduction reaction and antibacterial application. *Diam. Relat. Mater.* **2024**, *149*, 111560. [CrossRef]
38. Liu, Y.; Luo, S.; Yan, S. Green synthesis of reduced graphene oxide as high-performance electrode materials for supercapacitors. *Ionics* **2020**, *26*, 415–422. [CrossRef]
39. Cheng, Q.; Wang, Y.; Zhou, Q.; Duan, S.; Zhang, B.; Li, Y.; Zhang, L. The Green Synthesis of Reduced Graphene Oxide Using Ellagic Acid: Improving the Contrast-Enhancing Effect of Microbubbles in Ultrasound. *Molecules* **2023**, *28*, 7646. [CrossRef] [PubMed]
40. Shah, M.S.A.S.; Park, A.R.; Zhang, K.; Park, J.H.; Yoo, P.J. Green Synthesis of Biphasic TiO_2–Reduced Graphene Oxide Nanocomposites with Highly Enhanced Photocatalytic Activity. *ACS Appl. Mater. Interfaces* **2012**, *4*, 3893–3901. [CrossRef] [PubMed]
41. Chufa, B.M.; Gonfa, B.A.; Anshebo, T.Y.; Workneh, G.A. A Novel and Simplest Green Synthesis Method of Reduced Graphene Oxide Using Methanol Extracted Vernonia Amygdalina: Large-Scale Production. *Adv. Condens. Matter Physics* **2021**, *2021*, 6681710. [CrossRef]
42. Thiyagarajulu, N.; Deepak, P.; Kamaraj, C. Synthesis and characterization of reduced graphene oxide nanosheets using *Saraca indica* leaves and their antioxidant, antibacterial, and anticancer applications. *Biomass Conv. Bioref.* **2024**, *14*, 29515–29529. [CrossRef]
43. Perumal, D.; Albert, E.L.; Saad, N.; Hin, T.Y.Y.; Zawawi, R.M.; The, H.F.; Che Abdullah, C.A. Fabrication and Characterization of *Clinacanthus nutans* Mediated Reduced Graphene Oxide Using a Green Approach. *Crystals* **2022**, *12*, 1539. [CrossRef]
44. Manimaran, K.; Prakash, D.G.; Kumar, S. Biological approaches of reduced graphene oxide (rGO) nanosheets using *Pleurotus sajor caju* extract and its in vitro pharmaceutical applications. *Biomass Conv. Bioref.* **2024**, *14*, 27817–27827. [CrossRef]
45. Turunc, E.; Ulger, A.S.; Binzet, R. Green Synthesis of Reduced Graphene Oxide Decorated with Silver Nanoparticles Using *Onosma bracteosa* Leaf Extract for Efficient Electrochemical Detection of Hydrogen Peroxide. *Electrocatalysis* **2024**, *2*, 1–5. [CrossRef]
46. Dominic, R.M.; Punniyakotti, P.; Balan, B.; Angaiah, S. Green synthesis of reduced graphene oxide using *Plectranthus amboinicus* leaf extract and its supercapacitive performance. *Bull. Mater. Sci.* **2022**, *45*, 2. [CrossRef]
47. Shubha, P.; Namratha, K.; Aparna, H.S.; Ashok, N.R.; Mustak, M.S.; Chatterjee, J.; Byrappa, K. Facile green reduction of graphene oxide using *Ocimum sanctum* hydroalcoholic extract and evaluation of its cellular toxicity. *Mater. Chem. Phys.* **2017**, *198*, 66–72. [CrossRef]
48. Marcano, D.C.; Kosynkin, D.V.; Berlin, J.M.; Sinitskii, A.; Sun, Z.; Slesarev, A.; Alemany, L.B.; Lu, W.; Tour, J.M. Improved Synthesis of Graphene Oxide. *ACS Nano* **2010**, *4*, 4806–4814. [CrossRef]
49. Huang, H.-H.; De Silva, K.K.H.; Kumara, G.R.A.; Yoshimura, M. Structural Evolution of Hydrothermally Derived Reduced Graphene Oxide. *Sci. Rep.* **2018**, *8*, 6849. [CrossRef]
50. Díez, N.; Śliwak, A.; Gryglewicz, S.; Gryzb, B.; Gryglewicz, G. Enhanced reduction of graphene oxide by high-pressure hydrothermal treatment. *RSC Adv.* **2015**, *5*, 81831–81837. [CrossRef]
51. Mokoloko, L.L.; Forbes, R.P.; Coville, N.J. The Transformation of 0-D Carbon Dots into 1-, 2- and 3-D Carbon Allotropes: A Minireview. *Nanomaterials* **2022**, *12*, 2515. [CrossRef]
52. Ferrari, A.C.; Robertson, J. Interpretation of Raman spectra of disordered and amorphous carbon. *J. Phys. Rev. B* **2000**, *61*, 14095–14107. [CrossRef]
53. Ferrari, A.C.; Meyer, J.C.; Scaraci, V.; Casiraghi, C.; Lazzeri, M.; Mauri, F.; Piscanec, S.; Jiang, D.; Novoselov, K.S.; Roth, S.; et al. Raman Spectrum of Graphene and Graphene Layers. *Phys. Rev. Lett.* **2006**, *97*, 187401. [CrossRef]
54. Oliveira, A.E.F.; Braga, G.B.; Tarley, C.R.T.; Periera, A.C. Thermally reduced graphene oxide: Synthesis, studies and characterization. *J. Mater. Sci.* **2018**, *53*, 12005–12015. [CrossRef]
55. Park, O.-K.; Choi, Y.-M.; Hwang, J.Y.; Yang, C.-H.; Kim, T.-W.; You, N.-H.; Koo, H.Y.; Lee, J.H.; Ku, B.-C.; Goh, M. Defect healing of reduced graphene oxide via intramolecular cross-dehydrogenative coupling. *Nanotechnology* **2013**, *24*, 185604. [CrossRef]
56. Kaniyoor, A.; Ramaprabhu, S. A Raman spectroscopic investigation of graphite oxide derived graphene. *AIP Adv.* **2012**, *2*, 032183. [CrossRef]
57. Maddumage, D.C.; Panamaldeniya, S.A.; Kimbulapitiya, K.M.; Jayakantha, D.N.; Munasinghe, M.A.; Pemasiri, B.M.; Gunawardhana, N.; Dassanayake, B.S. Effect of annealing temperature on electrical properties of RGO thin films deposited by Atomized Spray Pyrolysis. *Diam. Relat. Mater.* **2021**, *120*, 108712. [CrossRef]
58. Du, D.; Li, P.; Ouyang, J. Nitrogen-Doped Reduced Graphene Oxide Prepared by Simultaneous Thermal Reduction and Nitrogen Doping of Graphene Oxide in Air and Its Application as an Electrocatalyst. *ACS Appl. Mater. Interfaces* **2015**, *7*, 26952–26958. [CrossRef]
59. Shen, X.; Lin, X.; Yousefi, N.; Jia, J.; Kim, J.-K. Wrinkling in graphene sheets and graphene oxide papers. *Carbon* **2014**, *66*, 84–92. [CrossRef]

60. Kumar, R.; da Silva, E.T.S.G.; Singh, R.K.; Savu, R.; Alaferdov, A.V.; Fonseca, L.C.; Carossi, L.C.; Singh, A.; Khandka, S.; Kar, K.K.; et al. Microwave-assisted synthesis of palladium nanoparticles intercalated nitrogen doped reduced graphene oxide and their electrocatalytic activity for direct-ethanol fuel cells. *J. Colloid Interface Sci.* **2018**, *515*, 160–171. [CrossRef] [PubMed]
61. Alazmi, A.; El Tall, O.; Rasul, S.; Hedhili, M.N.; Patole, S.P.; Costa, P.M. A process to enhance the specific surface area and capacitance of hydrothermally reduced graphene oxide. *Nanoscale* **2016**, *8*, 17782–17787. [CrossRef]
62. Li, Q.; Liu, J.; Bai, A.; Li, P.; Li, J.; Zhang, X.; Yu, M.; Wang, J.; Sun, H. Preparation of a Nitrogen-Doped Reduced Graphene Oxide-Modified Graphite Felt Electrode for $VO^{2+}/VO_2{}^{+}$ Reaction by Freeze-Drying and Pyrolysis Method. *J. Chem.* **2019**, *1*, 8958946. [CrossRef]
63. Phattharasupakun, N.; Wutthiprom, J.; Ma, N.; Suktha, P.; Sawangphruk, M. High-Performance Supercapacitors of N-Doped Graphene Aerogel and Its Nanocomposites with Manganese Oxide and Polyaniline. *J. Electrochem. Soc.* **2018**, *165*, A1430–A1439. [CrossRef]

Disclaimer/Publisher's Note: The statements, opinions and data contained in all publications are solely those of the individual author(s) and contributor(s) and not of MDPI and/or the editor(s). MDPI and/or the editor(s) disclaim responsibility for any injury to people or property resulting from any ideas, methods, instructions or products referred to in the content.